Journal of Materials Chemistry C

ROYAL SOCIETY OF CHEMISTRY

COMMUNICATION

View Article Online
View Journal | View Issue

Check for updates

Cite this: J. Mater. Chem. C, 2023, 11, 3715

Received 16th January 2023,
Accepted 23rd February 2023

DOI: 10.1039/d3tc00185g

rsc.li/materials-c

Published on 23 February 2023. Downloaded on 9/20/2024 12:31:46 AM.

# Hydrothermal synthesis of stable lead-free $Cs_4MnBi_2Cl_{12}$ perovskite single crystals for efficient photocatalytic degradation of organic pollutants†

Xiao-Feng Qi, Fei Zhang, Zhi-Peng Chen, Xu Chen, Mo-Chen Jia, Hui-Fang Ji* and Zhi-Feng Shi *

**Recently, the photocatalytic degradation of organic pollutants using halide perovskite materials has increasingly attracted people's attention. However, the stability issues and the lead toxicity of such materials cast a shadow over their practical applications. In this study, we successfully synthesized non-toxic $Cs_4MnBi_2Cl_{12}$ single crystals (SCs) using a hydrothermal method. Joint experiment–theory characterizations reveal the good stability of $Cs_4MnBi_2Cl_{12}$. Furthermore, the application of $Cs_4MnBi_2Cl_{12}$ as a photocatalyst in the degradation of organic pollutants was demonstrated for the first time. In detail, rhodamine B (RhB), methylene blue and Sudan Red III dissolved in ethanol can be degraded and decolorized by $Cs_4MnBi_2Cl_{12}$ SCs under light irradiation. About 97% RhB can be degraded in 7 min, and the degradation efficiency is hardly decreased over ten cycles. Besides, the photocatalytic degradation mechanisms were studied, and the results show that the superoxide ($^{\bullet}O_2^-$) plays a leading role in the photocatalytic process. The degradation pathways of organic pollutants were subsequently analyzed by high-performance liquid chromatography–mass spectrometry, involving three stages of *N*-deethylation, ring opening, and mineralization. Encouraged by the remarkable structural and optical stability of $Cs_4MnBi_2Cl_{12}$ SCs, such lead-free perovskite materials may have broad application prospects in the field of photocatalysis.**

## Introduction

Recently, with the rapid population growth and the development of global industrialization, the pollution of organic dyes has become increasingly high, which has damaged the ecosystem seriously and threatened the sustainable development of human society.[1] Under these circumstances, the development of advanced treatment technologies for organic pollutant degradation is an important pursuit and certainly a worthwhile subject. Solar energy is abundant, and has shown immense potential in tackling environmental problems and photocatalysis has proven to be effective in the degradation of organic dyes.[2] The photocatalytic reaction uses semiconductor materials as catalysts to degrade, decolorize, and detoxify macromolecular organic pollutants under sunlight, and convert them into inorganic small molecular substances, such as $CO_2$ and $H_2O$.[3] This treatment technology possesses the advantages of low energy consumption, simple operation, and mild reaction conditions.[4] Currently, the experimentally explored photocatalyst materials include metal oxides ($TiO_2$, ZnO, $SnO_2$, and $WO_3$),[5–7] metal sulfides (CdS, PbS, and ZnS),[8] nitrides ($C_3N_4$ and GaN),[9] phosphides (InP and GaP),[10,11] and so on. For example, Zhang synthesized a novel phosphorus (P)-doped fiber tubular graphitic carbon nitride (g-$C_3$N4)/g-$C_3N_4$/titanium nitride (TiN) composite (FCN/CN/TiN).[12] FCN/CN/TiN has been endowed with remarkably high photocatalytic performance with a degradation efficiency of 94%, and can still maintain the stability of the material and degradation efficiency after four cycles. Although the materials mentioned above have shown good performance in photocatalytic reactions, they still face some drawbacks including fast recombination rates of photo-generated carriers, low light utilization, complex preparation process, *etc.*[13–15] Therefore, from the application point of view, it is imperative to search for alternative semiconductor materials with a low carrier recombination rate and cost-effectiveness as photocatalysts to address the above issues.

In recent years, metal-halide perovskite materials have increasingly received attention due to their great capabilities in cost-effective and large-scale manufacturing in optoelectronic devices, including solar cells, photodetectors, lasers, and light-emitting diodes.[16–22] Compared to the intensive efforts in optoelectronic applications, the investigation of perovskites as photocatalysts in pollutant degradation is relatively less

*Key Laboratory of Materials Physics of Ministry of Education, School of Physics and Microelectronics, Zhengzhou University, Daxue Road 75, Zhengzhou, 450052, China. E-mail: shizf@zzu.edu.cn, jifang@zzu.edu.cn; Fax: +86-371-67766629; Tel: +86-150-9333-9165*

† Electronic supplementary information (ESI) available. See DOI: https://doi.org/10.1039/d3tc00185g

Published on 23 February 2023. Downloaded on 9/20/2024 12:31:46 AM.

intensive. In fact, the intrinsically large light absorption coefficient, long charge carrier lifetime, tunable bandgap, and solution-processed method provide metal-halide perovskites with broad prospects for high-performance photocatalysts, and much progress in this field has been witnessed in the past several years, including photocatalytic reduction of $CO_2$,[23] hydrogen production,[24] NO removal,[25] and organic pollutant degradation. For example, $CsPbX_3$ (X = Cl, Br) perovskite quantum dots (QDs) can decompose methyl orange (MO) solution into a colorless solution within 100 min.[26] The eosin-B dye can be degraded by $CsPbCl_3$ QDs under visible light irradiation within 140 min.[27] $CsPbBr_3$ nanocrystals can degrade methylene blue (MB) solution within 60 min, and the photocatalytic degradation rate is 99.18%.[28] Nevertheless, the inherent toxic element lead contained in lead-halide perovskites and their instability cast a shadow over their practical applications. Thanks to the rich combinatorial chemistry of perovskite materials, researchers have developed some stable and lead-free perovskite materials and applied them in organic pollutant degradation. For example, Bresolin *et al.* synthesized the $(CH_3NH_3)_3Bi_2I_9$ powder, which can effectively degrade Rhodamine B (RhB) and MB solutions under light irradiation.[29] Analogously, Akinbami *et al.* observed that $Cs_3Bi_2Br_9$ nanoparticles can be used for photocatalytic degradation of RhB and MB solutions.[30] Besides, $Cs_2AgInCl_6$ nanocrystals were used for photocatalytic degradation of Sudan Red III dyes, about 98.5% of Sudan Red III solution was degraded within 16 min.[31] Moreover, $Cs_2AgBiBr_6$ also has photocatalytic properties and can be used to degrade RhB solution, and the photocatalytic efficiency can be significantly improved when precious metals such as Pt and Au are deposited on its surface[32] while the above three lead-free perovskite materials are characterized by indirect bandgap nature, resulting in a low light utilization efficiency. Moreover, they all have relatively short carrier lifetimes, thus it is difficult to ensure that the photoexcited charge carriers have sufficient time to reach the active sites to complete the surface redox reaction.

In this study, we successfully synthesized the non-toxic and stable $Cs_4MnBi_2Cl_{12}$ single crystals (SCs) using a hydrothermal method, which are characterized by direct bandgap and long carrier lifetime. The $Cs_4MnBi_2Cl_{12}$ SCs can degrade and decolorize RhB, MB and Sudan Red III in ethanol-based photocatalytic systems, demonstrating a high degradation efficiency and stability. About 97% RhB can be degraded in 7 min, and the degradation efficiency does not decrease significantly after ten cycles. After the degradation process, the photocatalyst can be recovered by filtration and cleaning, showing the characteristics of convenient recovery, and high recovery and utilization rate. The photocatalytic degradation mechanisms show that the dye molecules have undergone the mineralization process, and the main active species are the superoxide radical ($^{\bullet}O_2^-$), and the degradation pathways of organic pollutants involve three stages of *N*-deethylation, ring opening, and mineralization. The above results show that the lead-free $Cs_4MnBi_2Cl_{12}$ SCs with a simple synthesis method and high degradation efficiency are safe and efficient photocatalytic materials.

## Results and discussion

In this work, the $Cs_4MnBi_2Cl_{12}$ perovskite SCs were synthesized using a slow cooling crystallization method, as schematically illustrated in Fig. 1a. Firstly, the mixture of CsCl, $MnCl_2$ and $BiCl_3$ were thoroughly ground. Then, the mixture was dissolved in HCl solution. After a continuous sintering at 180 °C for 12 h, $Cs_4MnBi_2Cl_{12}$ crystals can be precipitated by slowly cooling to room temperature at a cooling rate of 10 °C $h^{-1}$. Fig. 1b illustrates the schematic crystal structure of $Cs_4MnBi_2Cl_{12}$. One can see that $Cs_4MnBi_2Cl_{12}$ with the triangular $R\bar{3}m$ space group belongs to layered double perovskite structure, in which $Mn^{2+}$ and $Bi^{3+}$ cations coordinate with six $Cl^-$ to form two octahedral blocking units, and the $[MnCl_6]^{4-}$ octahedral layer is sandwiched between two $[BiCl_6]^{3-}$ layers by angle sharing to form a two-dimensional perovskite structure, which endows it with excellent stability and tunable photoelectric properties.[33,34] The triangular structural characteristics of the synthesized $Cs_4MnBi_2Cl_{12}$ SCs were experimentally confirmed by X-ray diffraction (XRD). As shown in Fig. 1c, the $Cs_4MnBi_2Cl_{12}$ SCs have only the diffraction patterns from {001} planes, belonging to a triangular $R\bar{3}m$ space group (cell parameters: $a = b = 7.5426$ Å, $c = 36.9150$ Å, $\alpha = \beta = 90°$, $\gamma = 120°$), and the full-width at half-maximum (FWHM) of (0012) diffraction peak reaches 0.12°, suggesting a high crystallinity. Fig. 1d displays the X-ray photoelectron spectrometer (XPS) survey spectrum of $Cs_4MnBi_2Cl_{12}$ SCs, where relevant signals of C, Cs, Mn, Bi, and Cl were confirmed, and the binding energy signals of Cs 3d, Mn 2p, Bi 4f, and Cl 2p were presented in Fig. S1 (ESI†) after calibrating with the C 1s peak at 284.57 eV. Fig. 1e and Fig. S2 (ESI†) show the typical scanning electron microscope (SEM) images of $Cs_4MnBi_2Cl_{12}$ crystals, which have a regular rhombic octahedral structure similar to that of double perovskites, and their surfaces are flat without obvious voids, which further indicates that the as-prepared samples have high crystallinity. Energy dispersive spectroscopy (EDS) elemental mapping analysis in Fig. 1f shows that Cs, Mn, Bi, and Cl elements are uniformly distributed in the octahedral microcrystal. Quantitative analysis of the EDS spectrum shown in Fig. S3 (ESI†) gives a quantified atomic ratio (%) of 8.90 : 1.95 : 3.97 : 23.13 (4.56 : 1 : 2.03 : 11.86) for Cs : Mn : Bi : Cl, which is close to the stoichiometry of the $Cs_4MnBi_2Cl_{12}$ material. Fig. 1g shows the high-resolution transmission electron microscope (TEM) image of the $Cs_4MnBi_2Cl_{12}$ crystal, and two sets of clear lattice fringes were identified with the interplanar spacings of 3.60 Å and 3.76 Å, corresponding to the (2$\bar{1}$3 and (2$\bar{1}$0 crystal planes of triangular $Cs_4MnBi_2Cl_{12}$. The corresponding Fourier transformation (FFT) image displayed in upper-right pane verifies the single-crystalline characteristics of the $Cs_4MnBi_2Cl_{12}$ crystal.

To understand the electronic structure of $Cs_4MnBi_2Cl_{12}$, the electronic band structure and density of states (DOS) of $Cs_4MnBi_2Cl_{12}$ were calculated by density functional theory (DFT).[35] As shown in Fig. 2a, $Cs_4MnBi_2Cl_{12}$ exhibits a direct bandgap at the F symmetry point with a bandgap energy of 3.22 eV. The corresponding DOS calculation in Fig. 2b shows that the conduction band minimum (CBM) of $Cs_4MnBi_2Cl_{12}$ is mainly composed of Bi 6p and Cl 3p orbitals, and its valence band maximum (VBM) mostly consists of Mn 3d and Cl 3p orbitals.

 This journal is © The Royal Society of Chemistry 2023

Published on 23 February 2023. Downloaded on 9/20/2024 12:31:46 AM.

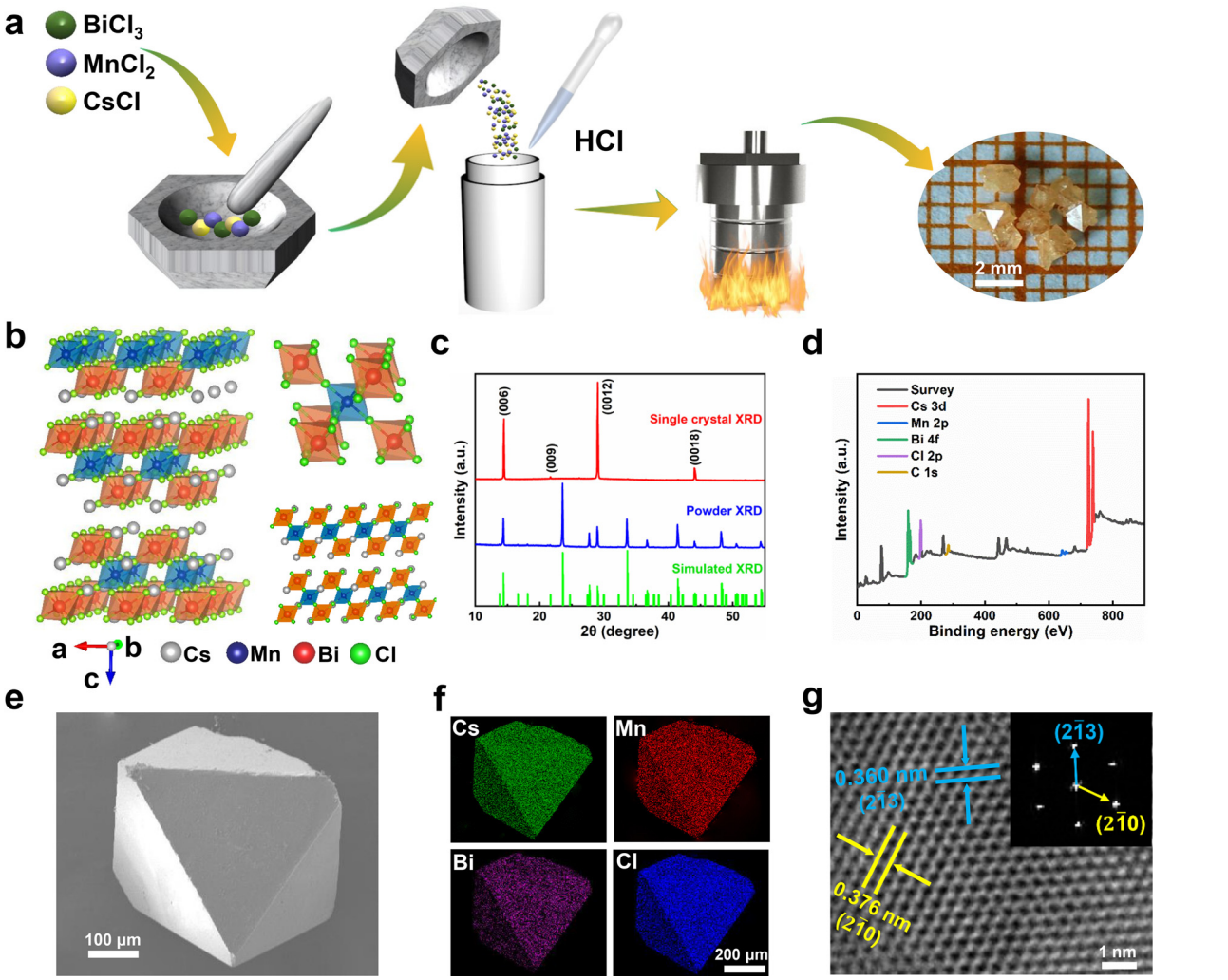


Fig. 1 (a) Schematic diagram of the synthesis process of $Cs_4MnBi_2Cl_{12}$ SCs. (b) Left: Schematic illustration of the crystal structure of $Cs_4MnBi_2Cl_{12}$. Right: Isolated two types of octahedral blocking units (top) and the crystal lattice view along the [110] direction (bottom). (c) XRD patterns of $Cs_4MnBi_2Cl_{12}$ SCs and powder. (d) XPS spectrum of $Cs_4MnBi_2Cl_{12}$ SCs. (e) SEM image of an individual $Cs_4MnBi_2Cl_{12}$ crystal, and (f) the corresponding EDS elemental distributions of Cs, Mn, Bi, and Cl, respectively. (g) High-resolution TEM images of $Cs_4MnBi_2Cl_{12}$ SCs. The inset shows the corresponding FFT patterns.

That is to say, the $[MnCl_6]^{4-}$ and $[BiCl_6]^{3-}$ polyhedra contribute the most electronic states in the energy band, and Cs contributes less to the CBM and the VBM. The isosurface plots of wave function $|\Psi|^2$ of the CBM and the VBM are shown in Fig. 2c and d, and the charge density is concentrated in $[MnCl_6]^{4-}$ and $[BiCl_6]^{3-}$ groups, isolated by $Cs^+$ ions.

The optical properties of $Cs_4MnBi_2Cl_{12}$ SCs were studied by ultraviolet-visible absorption and photoluminescence (PL). As shown in Fig. 2e, the $Cs_4MnBi_2Cl_{12}$ SCs have a broad absorption region (gray line), which start to absorb light at around 600 nm and have a strong absorption in the ultraviolet region.[36] Such a wide absorption region is conducive to absorbing more energy that supports efficient photodegradation. It should be mentioned that the strong absorption in the ultraviolet region comes from the $6s^2 \rightarrow 6s^16p^1$ transition of $Bi^{3+}$ ions.[37,38] A fully allowed $^1S_0 \rightarrow {}^1P_1$ transition is observed near 210 nm, and the peak at 267 nm belongs to $^1S_0 \rightarrow {}^3P_2$ forbidden transition, while the $^1S_0 \rightarrow {}^3P_1$ transition is responsible for the strong peaks at 330 and 352 nm. This splitting is due to the dynamic Jahn–Teller distortion effect of the excited state caused by the coupling of lattice vibration and Bi 6p–Cl 3p antibonding orbital coupling.[39] In addition, two weak absorption peaks at 430 and 515 nm were also detected in the visible region, corresponding to the spin-forbidden $^6A_1(S) \rightarrow {}^4T_1(G)$ and $^6A_1(S) \rightarrow {}^4T_2(G)$ d–d transitions of the $Mn^{2+}$, respectively.[40,41] From the Tauc plot analysis of the absorption spectra (Fig. S4, ESI†), the bandgap of $Cs_4MnBi_2Cl_{12}$ SCs is determined to be 3.01 eV, similar to that of the reported data.[36]

Preliminary optical studies (Fig. 2e, red line) show that the $Cs_4MnBi_2Cl_{12}$ SCs exhibit a strong and broad emission peak at 592 nm with a large FWHM of 75 nm, which is mainly caused by the spin-forbidden d–d transition ($^4T_1 \rightarrow {}^6A_1$) of paired $Mn^{2+}$ ion octahedra with magnetic coupling.[42] The inset of Fig. 2e displays a photograph of $Cs_4MnBi_2Cl_{12}$ SCs under ultraviolet light irradiation (365 nm), showing an intense orange–red light. To further confirm the emission mechanisms of $Cs_4MnBi_2Cl_{12}$,

Published on 23 February 2023. Downloaded on 9/20/2024 12:31:46 AM.

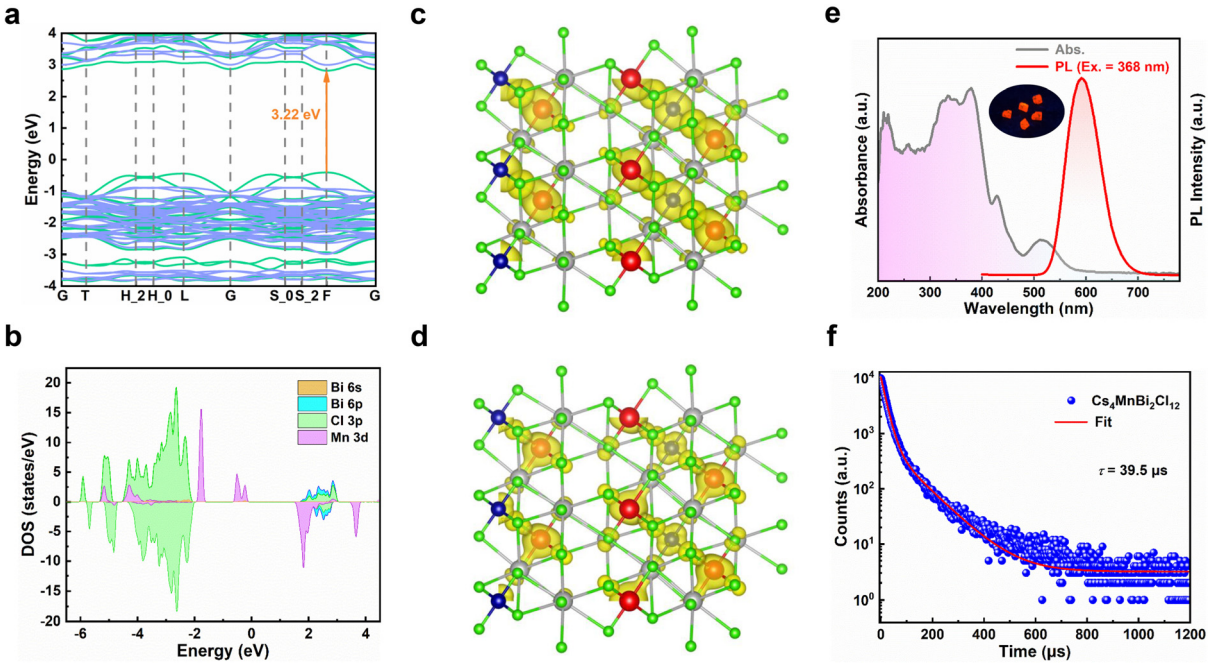


Fig. 2 (a) Calculated band structure, and (b) the corresponding DOS diagram of $Cs_4MnBi_2Cl_{12}$. The isosurface plots of the wave function $|\Psi|^2$ of (c) CBM and (d) VBM. (e) ultraviolet-visible absorption and PL spectra of $Cs_4MnBi_2Cl_{12}$ SCs. The inset shows the photograph of $Cs_4MnBi_2Cl_{12}$ SCs under ultraviolet light irradiation (365 nm). (f) Time-resolved PL decay curve of $Cs_4MnBi_2Cl_{12}$ SCs.

the PL spectra under different excitations and PL excitation (PLE) spectra under different emissions were measured. As shown in Fig. S5a (ESI†), the peak position and FWHM of the PL spectra show little dependence on the excitation wavelength ranging from 310 to 520 nm, suggesting that the broad red emission originates from the same radiative decay path rather than superposition of multiple defect recombination centers.[43] Likewise, the nondependence of PLE spectra (Fig. S5b, ESI†) on the emission wavelength also confirms that the orange–red emission originates from the relaxation of the same excited state—d–d transition of Mn ions.[36,44] In general, the PL intensity associated with the permanent defects in materials is characterized by a sublinear dependence on the excitation power, and an undesired emission saturation will occur when all defect states are filled.[45] However, in the present case, a linear relationship of excitation power-dependent PL eliminates the possibility of permanent defect-related transition (Fig. S6, ESI†). Transient-state PL measurements were also performed to gain more insight into the carrier recombination of $Cs_4MnBi_2Cl_{12}$ SCs. As shown in Fig. 2f, the PL decay curve of $Cs_4MnBi_2Cl_{12}$ SCs excited by 368 nm monitoring at 592 nm can be fitted by three exponential decay functions, and the average PL lifetime is about 39 μs, which is much larger than the conventional lead-halide perovskites and other lead-free metal halides.[46–50] Generally, the PL lifetime is inversely proportional to the density of trap states, where a longer lifetime is associated with less trap density. From the perspective of photocatalytic applications, a longer lifetime would reduce the possibility of carrier recombination, bringing about higher opportunity to degrade organic pollutants.[31] Moreover, the longer PL lifetime implies a lower charge carrier recombination rate, thus the photoexcited charge carriers would have sufficient time to reach the active sites to complete the surface redox reaction.[51]

The stability of photocatalysts is an important index to evaluate whether it can have commercial application, so we carried out a detailed study on the stability of $Cs_4MnBi_2Cl_{12}$ by combining theoretical and experimental analysis. First, the dynamic stability and thermodynamic stability of $Cs_4MnBi_2Cl_{12}$ were studied by the first-principles calculations. As shown in Fig. 3a, no negative frequencies were observed in the calculated phonon band structure, which verifies the dynamic stability of $Cs_4MnBi_2Cl_{12}$. Fig. 3b presents the first-principles molecular dynamics simulations at 300 K, and the small potential energy fluctuation implies a good thermodynamic stability of $Cs_4MnBi_2Cl_{12}$. Furthermore, we extended the theoretical investigation into the decomposition enthalpy of $Cs_4MnBi_2Cl_{12}$. As shown in Fig. 3c, the decomposition enthalpy of $Cs_4MnBi_2Cl_{12}$ is much larger than that of $CsPbBr_3$, $CsPb_2Br_5$, and other lead-free perovskite materials, indicating the better stability and greater advantages of $Cs_4MnBi_2Cl_{12}$ for practical photocatalytic applications. Experimentally, the thermogravimetric analysis shows that $Cs_4MnBi_2Cl_{12}$ SCs have a high thermal stability and exhibit no significant weight loss until 500 °C, as seen in Fig. 3d. Furthermore, we conducted the photostability test of the $Cs_4MnBi_2Cl_{12}$ SCs by continuously illuminating the sample using a 365 nm ultraviolet lamp. As shown in Fig. 3e and Fig. S7 (ESI†), the absorption and PL spectra of $Cs_4MnBi_2Cl_{12}$ SCs barely changed in terms of the spectral shape and peak intensity after 48 h of continuous irradiation, which suggests a good photostability of $Cs_4MnBi_2Cl_{12}$ SCs. Considering the strong dependence of organic pollutant degradation on the solution environment,

 This journal is © The Royal Society of Chemistry 2023

Published on 23 February 2023. Downloaded on 9/20/2024 12:31:46 AM.

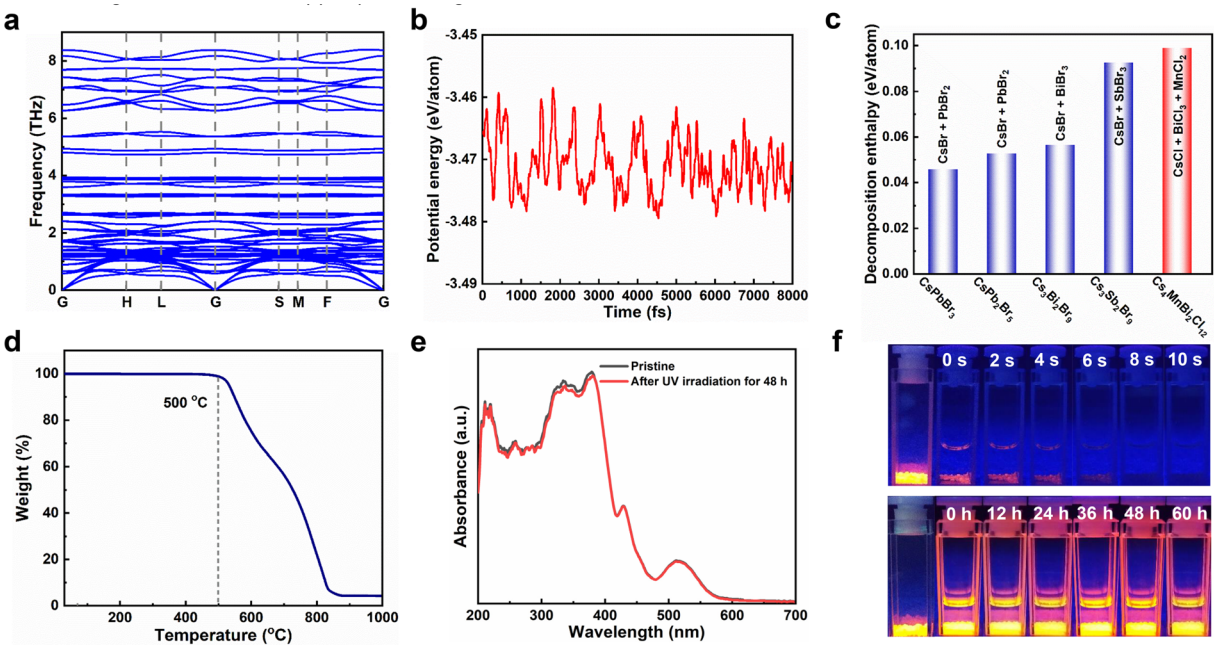


Fig. 3 (a) Phonon band structures of the $Cs_4MnBi_2Cl_{12}$. (b) Potential energy fluctuations of $Cs_4MnBi_2Cl_{12}$ as a function of the molecular dynamic simulation step at 300 K. (c) Comparison of the decomposition enthalpy of $Cs_4MnBi_2Cl_{12}$ with other halide perovskites. (d) Thermogravimetry analysis of the $Cs_4MnBi_2Cl_{12}$ SCs. (e) Absorption spectra of the $Cs_4MnBi_2Cl_{12}$ SCs before and after continuous ultraviolet light irradiation for 48 h. (f) Photographs of the $Cs_4MnBi_2Cl_{12}$ SCs soaked in water (upper) and alcohol (bottom) for different times.

another stability test of $Cs_4MnBi_2Cl_{12}$ SCs in different solvent environments was therefore conducted. Generally, water was deemed to be one of the fatal factors for conventional lead-halide perovskites, which are easily decomposed once exposed to water because of the hygroscopic halide salts.[52] To evaluate the stability of $Cs_4MnBi_2Cl_{12}$ SCs against water corrosion, the as-synthesized sample was therefore soaked in deionized water. As we expected, the $Cs_4MnBi_2Cl_{12}$ SCs experienced a rapid fluorescence quenching in water environment and lost most of the brightness within 10 s of standing, as shown in the upper pane of Fig. 3f, which may be induced by the ionic nature of $Cs_4MnBi_2Cl_{12}$. In sharp contrast, when we replaced the deionized water with alcohol, the bright orange–red luminescence typical to $Cs_4MnBi_2Cl_{12}$ SCs can be stabilized even with a long-standing time for 60 h (bottom pane). Therefore, for stable and reproducible photocatalytic degradation by using $Cs_4MnBi_2Cl_{12}$, alcohol is a very reliable solvent of choice. The above experimental results indicate the remarkable stability of the $Cs_4MnBi_2Cl_{12}$ system, making it suitable as an environmentally friendly photocatalyst for the degradation of organic pollutants in ethanol.

The photocatalytic activity of $Cs_4MnBi_2Cl_{12}$ SCs was experimentally evaluated by removing three organic dyes (RhB, MB, and Sudan III) in ethanol solution under a 300 W mercury lamp irradiation. Fig. 4a–c present a series of ultraviolet-visible absorption spectra of RhB, MB, and Sudan Red III at different irradiation times in the presence of $Cs_4MnBi_2Cl_{12}$, and regular spectral evolution was revealed. Specifically, the absorption peak intensity of RhB decreases dramatically with increasing the irradiation time (Fig. 4a). Within a short period of 7 min, the characteristic absorption peak of RhB almost disappears, with a degradation rate as high as 97%, which suggests that the RhB solution was almost completely degraded. The inset of Fig. 4a presents the change of RhB solution color with different irradiation times, showing a regular change from dark purple to transparent. To verify the positive role of $Cs_4MnBi_2Cl_{12}$ in the RhB degradation process, the control experiments were conducted. As shown in Fig. S8 (ESI†), RhB is hardly degraded under a mercury lamp irradiation without the $Cs_4MnBi_2Cl_{12}$ catalyst. Also, RhB is difficult to be degraded with catalyst under dark conditions. These results indicate that $Cs_4MnBi_2Cl_{12}$ is the real factor to enable degradation of RhB. For the other organic pollutants, the effect of photodegradation is also significant. As shown in Fig. 4b and c, MB and Sudan Red III dyes with the same concentration as RhB were employed for the identical experiments, and the regular color changes from blue cyan (MB) and orange (Sudan Red III) to transparent lend support to the view of almost complete degradation. In detail, the degradation rates of MB and Sudan III were 98.3% and 97.4%, respectively, within 16 min. The above results demonstrate that $Cs_4MnBi_2Cl_{12}$ SCs show high photocatalytic activity for different dyes, among which the degradation performance of RhB is the best (Fig. 4d), so we will focus on RhB as the main research object in the following research. Subsequently, the degradation rates of RhB with different addition amounts of $Cs_4MnBi_2Cl_{12}$ catalysts were investigated to describe the kinetics of the photocatalytic reaction. As shown in Fig. 4e, with the increase of catalyst content, the degradation rate of RhB first increases and then decreases, and the degradation rate reaches its maximum when the catalyst content is 5 mg. The Langmuir Hinshelwood (L–H) model can be used to describe the degradation rate under

Published on 23 February 2023. Downloaded on 9/20/2024 12:31:46 AM.

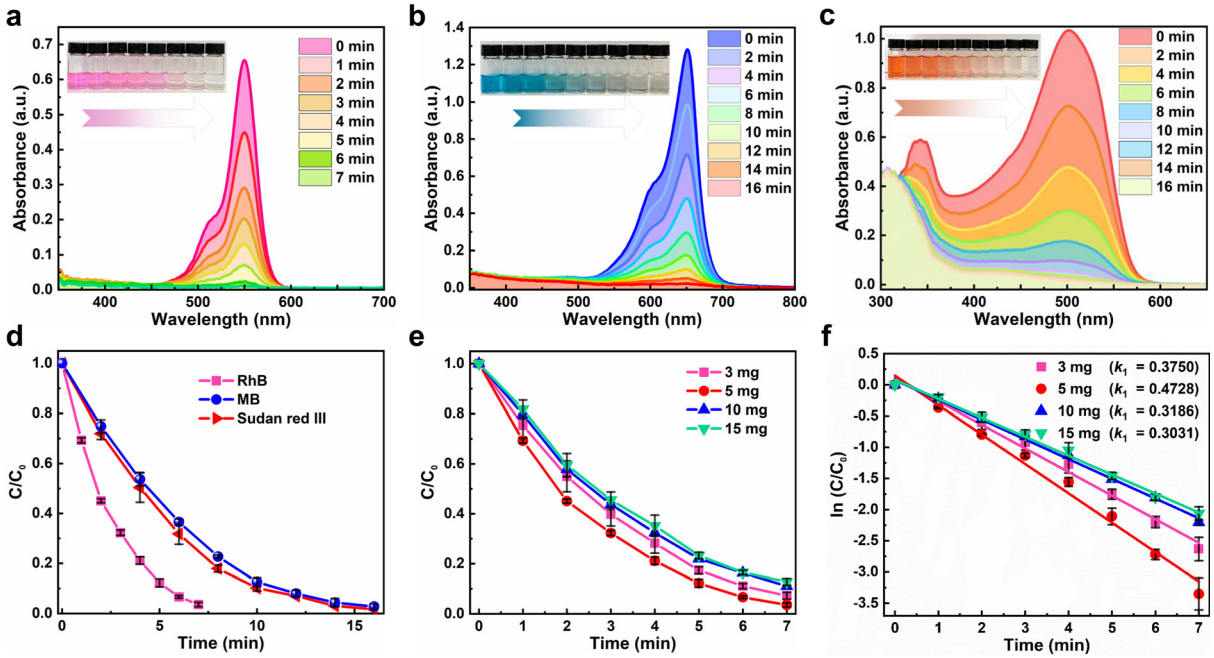


Fig. 4 Ultraviolet-visible absorption spectra of (a) RhB, (b) MB, and (c) Sudan Red III at different irradiation times in the presence of $Cs_4MnBi_2Cl_{12}$. The insets show the change of solution color with time. (d) Plots of $C/C_0$ *versus* the irradiation time for the degradation of RhB, MB, and Sudan Red III dyes. (e) Plots of $C/C_0$ *versus* the irradiation time for the degradation of RhB with different catalyst addition amount. (f) Corresponding reaction kinetic curves of the RhB degradation fitted using the first-order model.

different catalyst contents more intuitively, in which the first-order model is expressed as $-\ln(C_t/C_o) = k_1 t + b$, where $C_0$ is the initial concentration of dye, $C_t$ is the concentration of dye under different degradation reaction times $t$, $k_1$ is the first-order rate constant and $b$ is a constant. By fitting the data, it can be found that the calculated $k_1$ increases from 0.3914 to 0.4737 $min^{-1}$ when the addition amount of $Cs_4MnBi_2Cl_{12}$ increases from 3 to 5 mg (Fig. 4f), implying that the degradation rate increases with the increase of catalyst content, which is mainly because of the number of active sites available for adsorption that are proportional to the catalyst content. Theoretically, more catalyst addition means larger exposure area to light, and thus more reactive species (free radicals) can be produced.[53,54] However, further increasing the catalyst content to 10 mg and above, light penetration through the solution would be inhibited due to an enhanced light scattering.[55,56] As a result, the degradation rate of RhB decreases rather than increases. Table S1 (ESI†) summarizes the photocatalytic properties of $Cs_4MnBi_2Cl_{12}$ and other perovskite materials. By comparison, the $Cs_4MnBi_2Cl_{12}$ has a more superior photocatalytic activity.

It is well known that the sustainability of photocatalysts plays a key role in their practical applications. In the present case, the sustainability of the $Cs_4MnBi_2Cl_{12}$ photocatalyst was examined by performing continuous ten cycles of RhB degradation under the same conditions (air ambient, 30 °C, 50% humidity). As shown in Fig. 5a, the photocatalytic degradation time of $Cs_4MnBi_2Cl_{12}$ SCs can be well maintained for 7 min over a ten cycle test; ten plotted curves repeat well and exhibit a reproducible response with time, indicating that the $Cs_4MnBi_2Cl_{12}$ photocatalyst has a good cycling stability. From the application point of view, a robust cycling stability of catalysts can effectively reduce the cost of photocatalysis, opening opportunities for future practical applications. It is worth mentioning that such good sustainability is greatly superior to the lead-halide perovskite catalysts ($CsPbBr_3$) reported by Fan *et al.*,[57] where the photocatalytic efficiency of $CsPbBr_3$ decays significantly over four cycles and the crystallinity of the recycled photocatalyst deteriorates seriously. Excitingly, this is not the case in our experiment. By comparing the XRD patterns of $Cs_4MnBi_2Cl_{12}$ SCs before and after photocatalysis (Fig. 5b), one can observe that, after ten successive degradation cycles, the structural integrity of $Cs_4MnBi_2Cl_{12}$ SCs was preserved well without the appearance of other additional diffractions, indicating that the photocatalyst is not decomposed even after ten photocatalytic cycles. Not only that, the $Cs_4MnBi_2Cl_{12}$ photocatalyst, without any encapsulation and protection, also demonstrates a robust stability against oxygen and moisture degradation. As shown in Fig. 5c, after long-term storage for three months in ambient air, the $Cs_4MnBi_2Cl_{12}$ SCs are able to maintain a good phase purity without the appearance of an impurity phase. Even if the $Cs_4MnBi_2Cl_{12}$ SCs were re-used for photocatalytic experiment after being stored in air for three months, the degradation rate of RhB is not much different from before, as seen in Fig. 5d. Therefore, in terms of material stability, the $Cs_4MnBi_2Cl_{12}$ possesses admirable and obvious advantages compared with other perovskite counterparts. This is no doubt the crucially important reason that ensuring the excellent sustainability of the photocatalytic degradation process. Furthermore, we investigated the effect of the size of $Cs_4MnBi_2Cl_{12}$ on the degradation rate. As shown in Fig. S9a (ESI†), the photocatalytic experiments were carried out with $Cs_4MnBi_2Cl_{12}$ powder

 This journal is © The Royal Society of Chemistry 2023

Published on 23 February 2023. Downloaded on 9/20/2024 12:31:46 AM.

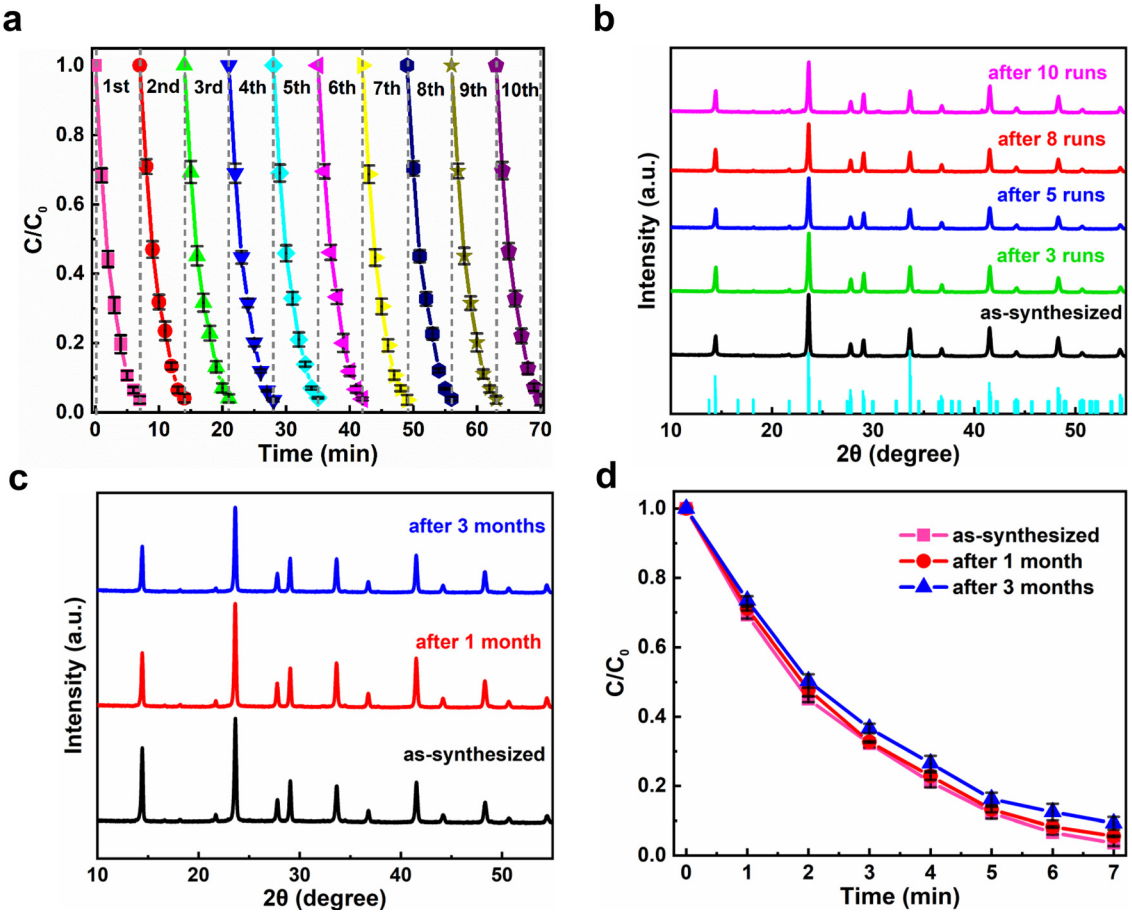


Fig. 5 (a) Ten successive degradation cycle test of $Cs_4MnBi_2Cl_{12}$ SCs under light irradiation in photocatalytic degradation of RhB. (b) XRD patterns of $Cs_4MnBi_2Cl_{12}$ SCs before and after degradation cycle tests. (c) XRD patterns of $Cs_4MnBi_2Cl_{12}$ after storage in air for one month and three months. (d) Plots of $C/C_0$ *versus* the irradiation time for the degradation of RhB with $Cs_4MnBi_2Cl_{12}$ SCs after storage in air for one month and three months.

and SCs, respectively. When the same mass of $Cs_4MnBi_2Cl_{12}$ powder and SCs were used to degrade 10 mg $L^{-1}$ of RhB dye, it can be found that the degradation rate of the powder is faster than that of the SCs, and the degradation can be completed in 6 min. In addition, photocatalytic cycling experiments were carried out with $Cs_4MnBi_2Cl_{12}$ powder, as shown in Fig. S9b (ESI†), RhB could be completely degraded within 6 min of the first two cycles, but the time for complete degradation of RhB was gradually prolonged as the number of cycles continued to increase, which may be caused by the decomposition of $Cs_4MnBi_2Cl_{12}$ powder after multiple degradation cycles. To confirm our suspicions, we monitored the XRD of $Cs_4MnBi_2Cl_{12}$ powder under different cycles, as shown in Fig. S9c (ESI†), a small amount of the $BiCl_3$ impurity phase appeared in the XRD patterns after the third cycle of catalytic testing, and the impurity peak of $BiCl_3$ after the fifth cycle increased, indicating that the $Cs_4MnBi_2Cl_{12}$ powder is easily decomposed into $BiCl_3$ after multiple cycles, which is also the reason for the decrease in the degradation rate after multiple cycles. In contrast, although the degradation rate of $Cs_4MnBi_2Cl_{12}$ SCs is slightly smaller than that of $Cs_4MnBi_2Cl_{12}$ powder, $Cs_4MnBi_2Cl_{12}$ SCs show better cycle stability, which is more suitable for practical applications in photocatalytic degradation. Therefore, we use $Cs_4MnBi_2Cl_{12}$ SCs for photocatalytic experiments. The above results and discussions fully reflect the great application prospects of stable $Cs_4MnBi_2Cl_{12}$ SCs in photocatalysis fields. The above results and discussions fully reflect the great application prospects of stable $Cs_4MnBi_2Cl_{12}$ in photocatalysis fields.

Generally, during the photocatalytic reaction, electrons ($e^-$), holes ($h^+$), hydroxyl radical ($^\bullet OH$) and superoxide ($^\bullet O_2^-$) may exist as the active species.[58] To examine the photocatalytic mechanisms, we therefore conducted the active radical capture experiments to identify the active species that re account for the degradation process. Fig. 6a plots the $C/C_0$ *versus* the irradiation time for the degradation of RhB with the addition of the free radical scavenger 2,2′,6,6′-tetramethylpiperidine-1-oxyl (TEMPO). One can observe that the photocatalytic degradation of dyes can be almost completely blocked after the TEMPO was added, suggesting that the photocatalytic degradation of dyes is a free radical-based process.[59] That is to say, three active radicals including hydroxyl radical ($^\bullet OH$), superoxide ($^\bullet O_2^-$) and holes ($h^+$) may involve in this photocatalytic degradation.[60] Since ethanol can capture $h^+$ active free radicals in the photocatalytic reaction, the most likely free radicals involved should be $^\bullet OH$ and $^\bullet O_2^-$.[61] To further make certain which free radical works, we add *p*-benzoquinone (*p*-BQ, $^\bullet O_2^-$ scavenger) and isopropanol (IPA, $^\bullet OH$ scavenger) to the ethanol solution of RhB for photocatalytic

Published on 23 February 2023. Downloaded on 9/20/2024 12:31:46 AM.

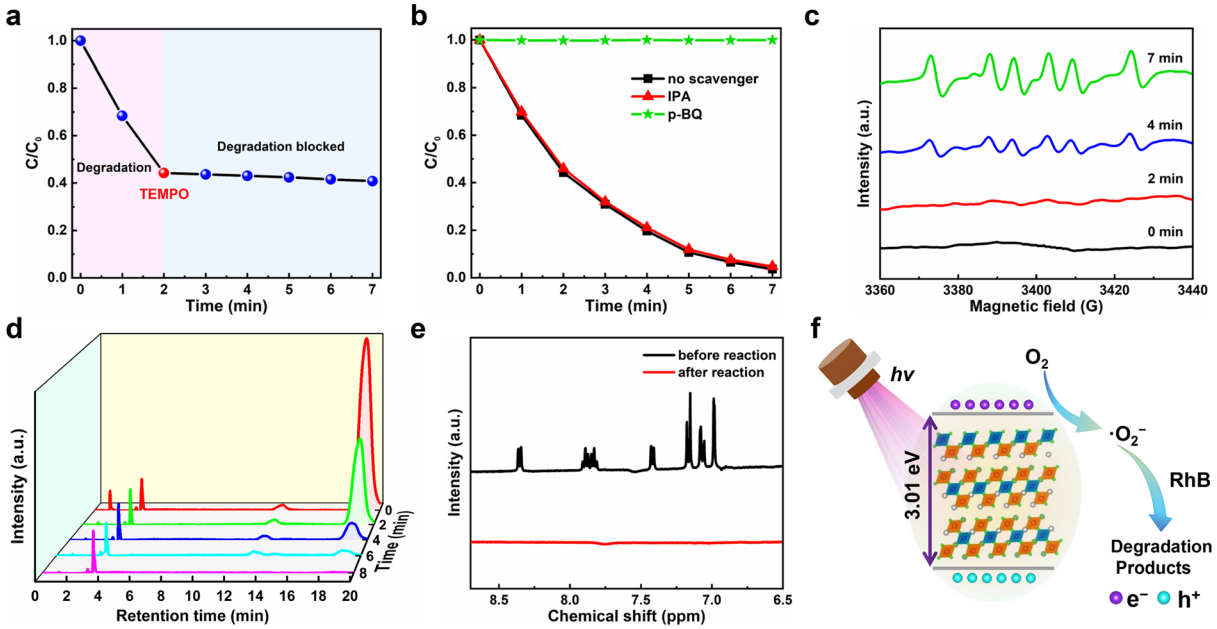


Fig. 6 Plots of $C/C_0$ *versus* the irradiation time for the degradation of RhB (a) with the addition of TEMPO during the illumination, and (b) in the presence of different scavengers. (c) The DMPO spin-trapping EPR spectra of $Cs_4MnBi_2Cl_{12}$ for $^{\bullet}O_2^-$ under different light irradiation times. (d) HPLC spectra of RhB monitored at 550 nm *versus* the retention time. (e) $^1$H NMR analysis of RhB before and after photocatalysis. (f) Schematic of mechanisms for the photocatalytic reaction of RhB under light irradiation.

experiments, and their effects on the photocatalytic degradation efficiency of RhB were measured and compared. As shown in Fig. 6b, the IPA addition has little effect on the photocatalytic degradation of RhB, indicating that $^{\bullet}OH$ does not participate in the degradation process. On the contrary, when *p*-BQ was added, the photocatalytic degradation was completely blocked, which suggests that $^{\bullet}O_2^-$ plays an important role in the degradation process. Moreover, we conducted the electron paramagnetic resonance (EPR) spectra test at room temperature to further verify the existence of $^{\bullet}O_2^-$ in the photocatalytic system, in which 5,5′-dimethyl-1-pyroline-*N*-oxide (DMPO) was used as the spin trapper. As shown in Fig. 6c, no signal of $^{\bullet}O_2^-$ was observed under dark conditions, but the characteristic peaks of $^{\bullet}O_2^-$ began to appear after the light irradiation for 2 min. With the increase of illumination time, the intensity of characteristic peaks also increases, which suggests that more $^{\bullet}O_2^-$ is produced under added light irradiation. The above observations show that $^{\bullet}O_2^-$ plays a leading role in the photocatalytic process, which is consistent with the results of active radical capture experiments discussed above.

The degradation process of RhB was further studied by high-performance liquid chromatography (HPLC). As shown in Fig. 6d, with the increase of radiation time, the characteristic HPLC peak of RhB at $t_R$ = 19.0 min gradually decreased and finally disappeared and no obvious new HPLC peaks appeared, which is consistent with the evolution trend of the ultraviolet-visible absorption spectra over the degradation process of RhB. Besides, the products after photocatalysis were examined by 1H nuclear magnetic resonance ($^1$H NMR). As shown in Fig. 6e, compared with the RhB dye before photocatalysis, it was found that the characteristic peaks of H in the benzene rings of RhB dye molecules between 6.5 ppm and 9 ppm completely disappeared after photocatalysis, which proved the decomposition of the benzene ring in RhB; in other words, the complete degradation of RhB. Based on the analysis of the above experimental results, we propose the photocatalytic mechanisms of superoxide radical (Fig. 6f), and the main reaction processes for RhB degradation are described as follows:

$$Cs_4MnBi_2Cl_{12} + RhB \rightarrow Cs_4MnBi_2Cl_{12} - RhB\ (RhB^*) \quad (1)$$

$$Cs_4MnBi_2Cl_{12} + h\nu \rightarrow h^+ + e^- \quad (2)$$

$$e^- + O_2 \rightarrow {}^{\bullet}O_2^- \quad (3)$$

$$^{\bullet}O_2^- + RhB^* \rightarrow \text{degradation products} \quad (4)$$

in which, RhB* means the activated dye molecules by $Cs_4MnBi_2Cl_{12}$. First, $Cs_4MnBi_2Cl_{12}$ activates the dye during the adsorption–desorption equilibrium process. Then, under UV light irradiation with photon energy higher than or equal to the bandgap of $Cs_4MnBi_2Cl_{12}$, electron in the valence band (VB) of $Cs_4MnBi_2Cl_{12}$ can be excited to the conduction band (CB), resulting in photogenerated $e^-$ and $h^+$. The electrons are captured by oxygen molecules adsorbed on the surface of catalyst particles or dissolved in solution to produce $^{\bullet}O_2^-$ free radicals, which then react with the activated dyes to form mineralized products. Note that the long carrier lifetime of $Cs_4MnBi_2Cl_{12}$ would contribute to the accumulation of $^{\bullet}O_2^-$ active radicals on its surface, providing more chance to degrade RhB dyes, thereby resulting in excellent photocatalytic activity.

In order to further determine the degradation pathway of RhB, the reaction solution was analyzed by HPLC–MS. Fig. S10 (ESI†) presents a series of MS spectra of the intermediates

 This journal is © The Royal Society of Chemistry 2023

Published on 23 February 2023. Downloaded on 9/20/2024 12:31:46 AM.

during RhB degradation, and their corresponding molecular formula are shown in Table S2 (ESI†). Based on the detected intermediates, we illustrated the possible degradation pathway of RhB. As shown in Fig. 7, in the photocatalytic degradation of RhB, *N*-deethylation was the main step leading to the production of series of intermediates.[62,63] Since the C–N bond in the whole RhB molecule is the most unstable,[64] it is most likely to be oxidized, broken and removed. Considering that there are two positions of C–N substituents in RhB molecule, so two ways of breaking exist. Firstly, RhB molecule was attacked by the photo-generated active radical ($^{\bullet}O_2^-$), which showed the breaking of C–N bond and *N*-deethylation to obtain the product with *m*/*z* = 415. It continues to show the fracture of C–N bond, *N*-deethylation to obtain the products with *m*/*z* values = 387, 359 and 331. Note that the above degradation path shows a continuous process of *N*-deethylation. The further oxidative degradation of product with *m*/*z* = 331 showed an oxidative ring opening process,[65] and thus the products with *m*/*z* = 139 and 154 were obtained. Finally, these compounds were further degraded into small molecular compounds and eventually mineralized into $CO_2$, $H_2O$, $NO_3^-$ and $NH_4^+$. To sum up, the photocatalytic degradation pathway of RhB dye by $Cs_4MnBi_2Cl_{12}$ SCs mainly includes three stages: *N*-deethylation, ring opening, and mineralization.

## Conclusions

In conclusion, an alcohol based photocatalytic system was successfully developed based on non-toxic $Cs_4MnBi_2Cl_{12}$ for the first time. The as-prepared $Cs_4MnBi_2Cl_{12}$ SCs have the octahedral shape with excellent crystallization. Joint experiment–theory characterizations confirm the good thermal and light stability of $Cs_4MnBi_2Cl_{12}$. Under light irradiation, the $Cs_4MnBi_2Cl_{12}$ SCs exhibit an excellent photocatalytic activity, which could degrade ~97% organic dye RhB within only 7 min, and the degradation efficiency has hardly decreased over ten successive cycles. Even after the $Cs_4MnBi_2Cl_{12}$ catalysts were stored in ambient air for three months, they could function properly and the degradation rate can be almost maintained. Moreover, we investigated the photocatalytic mechanism and degradation pathway of RhB in the present system. The results reveal that the $^{\bullet}O_2^-$ active radical plays a leading role in the photocatalytic process and the degradation pathway involves three stages of *N*-deethylation,

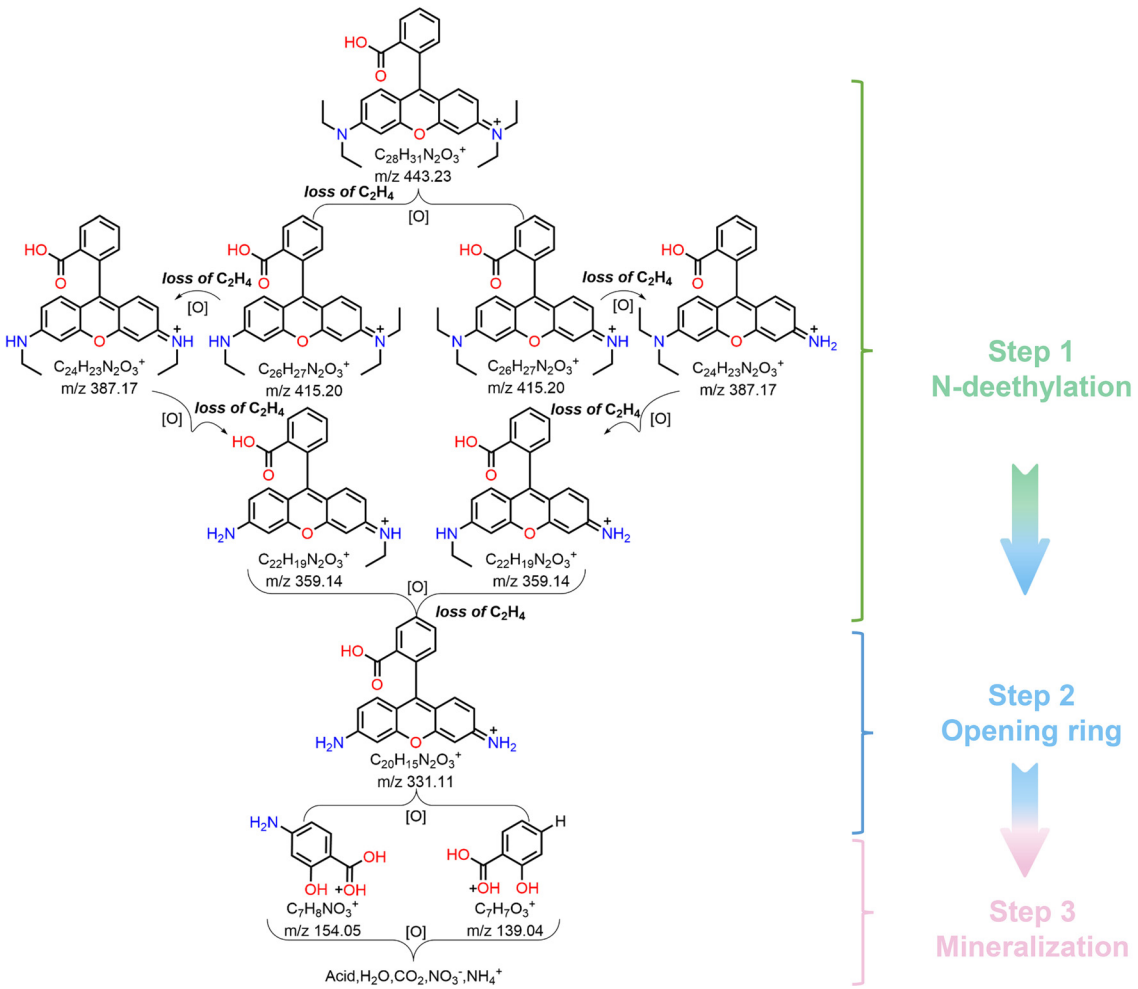


Fig. 7 Photocatalytic degradation pathways of RhB dye under light irradiation.

Published on 23 February 2023. Downloaded on 9/20/2024 12:31:46 AM.

ring opening, and mineralization. The nontoxicity, high photocatalytic efficiency, and robust stability of such $Cs_4MnBi_2Cl_{12}$ crystals make their future application in photocatalysis field a real possibility.

## Conflicts of interest

There are no conflicts to declare.

## Acknowledgements

The authors acknowledge financial support from the National Natural Science Foundation of China (No. 12074347, 12004346, 61935009 and 12204426), the Science Foundation for Distinguished Young Scholars of Henan Province (No. 212300410019), the Support Program for Scientific and Technological Innovation Teams of Higher Education in Henan Province (No. 23IRTSTHN011), and the Open Fund of the State Key Laboratory of Integrated Optoelectronics (IOSKL2020KF04).

## Notes and references

1 M. G. Walter, E. L. Warren, J. R. McKone, S. W. Boettcher, Q. Mi, E. A. Santori and N. S. Lewis, *Chem. Rev.*, 2010, **110**, 6446–6473.
2 Y. Tachibana, L. Vayssieres and J. Durrant, *Nat. Photonics*, 2012, **6**, 511–588.
3 W. Zhao, M. Adeel, P. Zhang, P. Zhou, L. Huang, Y. Zhao, M. A. Ahmad, N. Shakoor, B. Lou, Y. Jiang, I. Lynch and Y. Rui, *Environ. Sci.: Nano*, 2022, **9**, 61–68.
4 P. T. Anastas and M. M. Kirchhoff, *Acc. Chem. Res.*, 2002, **35**, 686–694.
5 Y. Liu, M. Zhang, C. H. Tung and Y. Wang, *ACS Catal.*, 2016, **6**, 8389–8394.
6 C. B. Ong, L. Y. Ng and A. W. Mohammad, *Renewable Sustainable Energy Rev.*, 2018, **81**, 536–551.
7 Y. He, L. Zhang, M. Fan, X. Wang, M. L. Walbridge, Q. Nong, Y. Wu and L. Zhao, *Sol. Energy Mater. Sol. Cells*, 2015, **137**, 175–184.
8 J. Yang, H. Yan, X. Wang, F. Wen, Z. Wang, D. Fan, J. Shi and C. Li, *J. Catal.*, 2012, **290**, 151–157.
9 B. AlOtaibi, S. Fan, D. Wang, J. Ye and Z. Mi, *ACS Catal.*, 2015, **5**, 5342–5348.
10 S. Yu, X.-B. Fan, X. Wang, J. Li, Q. Zhang, A. Xia, S. Wei, L.-Z. Wu, Y. Zhou and G. R. Patzke, *Nat. Commun.*, 2018, **9**, 4009.
11 D. B. Grotjahn, V. M. Soto, E. J. Kragulj, D. A. Lev, G. Erdogan, X. Zeng and A. L. Cooksy, *J. Am. Chem. Soc.*, 2008, **130**, 6342–6344.
12 M. J. Zhang, L. Tang, A. Duan, Y. Zhang, F. J. Xiao, Y. Zhu, J. J. Wang, C. Y. Fang and N. Yin, *Chem. Eng. J.*, 2023, **452**, 139068.
13 J. Qiu, X. Zhang, Y. Feng, X. Zhang, H. Wang and J. Yao, *Appl. Catal., B*, 2018, **231**, 317–342.
14 M. Ge, Q. Li, C. Cao, J. Huang, S. Li, S. Zhang, Z. Chen, K. Zhang, S. S. Al-Deyab and Y. Lai, *Adv. Sci.*, 2017, **4**, 1600152.
15 M. Sharma, T. Jain, S. Singh and O. P. Pandey, *Sol. Energy*, 2012, **86**, 626–633.
16 H. Cho, S. H. Jeong, M. H. Park, Y. H. Kim, C. Wolf, C. L. Lee, J. H. Heo, A. Sadhanala, N. Myoung, S. Yoo, S. H. Im, R. H. Friend and T. W. Lee, *Science*, 2015, **350**, 1222–1225.
17 Y. H. Kim, H. Cho and T. W. Lee, *Proc. Natl. Acad. Sci. U. S. A.*, 2016, **113**, 11694–11702.
18 J. Y. Kim, J. W. Lee, H. S. Jung, H. Shin and N. G. Park, *Chem. Rev.*, 2020, **120**, 7867–7918.
19 Y. H. Kim, H. Cho, J. H. Heo, T. S. Kim, N. Myoung, C. L. Lee, S. H. Im and T. W. Lee, *Adv. Mater.*, 2015, **27**, 1248–1254.
20 F. Zhang, B. Yang, Y. Li, W. Deng and R. He, *J. Mater. Chem. C*, 2017, **5**, 8431–8435.
21 X. Yang, Y. Fu, R. Su, Y. Zheng, Y. Zhang and W. Yang, *Adv. Mater.*, 2020, **32**, 2002585.
22 C. Lin, S. Li, W. Zhang, C. Shao and Z. Yang, *ACS Appl. Energy Mater.*, 2018, **1**, 1374–1380.
23 S. Kumar, M. Regue, M. A. Isaacs, E. Freeman and S. Eslava, *ACS Appl. Energy Mater.*, 2020, **3**, 4509–4522.
24 Z. He, Q. Tang, X. Liu, X. Yan, K. Li and D. Yue, *Energy Fuels*, 2021, **35**, 15005–15009.
25 B. Huo, J. Yang, Y. Bian, D. Wu, J. Feng, J. Zhou, Q. Huang, F. Dong and X. Tang, *Chem. Eng. J.*, 2021, **406**, 126740.
26 S. Das, T. Paul, S. Maiti and K. K. Chattopadhyay, *Mater. Lett.*, 2020, **267**, 127501.
27 Q. Zhang, X. Deng, C. Tan, Y. Zhou, X. Chen, X. Bai, J. Li, B. Tang, S. Li and H. Lin, *J. Chem. Phys.*, 2020, **153**, 024703.
28 Y. Zhao, H. Shi, X. Hu, E. Liu and J. Fan, *Chem. Eng. J.*, 2020, **381**, 122692.
29 B. M. Bresolin, S. B. Hammouda and M. Sillanpää, *J. Photochem. Photobiol., A*, 2019, **376**, 116–126.
30 O. Akinbami, R. Moepya, G. N. Ngubeni, P. Tetyana, K. P. Mubiayi, M. J. Moloto and N. Moloto, *J. Photochem. Photobiol., A*, 2021, **419**, 113460.
31 K. Li, S. Li, W. Zhang, Z. Shi, D. Wu, X. Chen, P. Lin, Y. Tian and X. Li, *J. Colloid Interface Sci.*, 2021, **596**, 376–383.
32 Z. Zhang, Y. Liang, H. Huang, X. Liu, Q. Li, L. Chen and D. Xu, *Angew. Chem., Int. Ed.*, 2019, **58**, 7263–7267.
33 B. Vargas, R. Torres-Cadena, D. T. Reyes-Castillo, J. Rodríguez-Hernández, M. Gembicky, E. Menéndez-Proupin and D. Solis-Ibarra, *Chem. Mater.*, 2019, **32**, 424–429.
34 B. Vargas, R. Torres-Cadena, J. Rodríguez-Hernández, M. Gembicky, H. Xie, J. Jiménez-Mier, Y.-S. Liu, E. Menéndez-Proupin, K. R. Dunbar, N. Lopez, P. Olalde-Velasco and D. Solis-Ibarra, *Chem. Mater.*, 2018, **30**, 5315–5321.
35 F. Zhang, Z. Ma, Z. Shi, X. Chen, D. Wu, X. Li and C. Shan, *Energy Mater. Adv.*, 2021, 5198145.
36 J. H. Wei, J. F. Liao, X. D. Wang, L. Zhou, Y. Jiang and D. B. Kuang, *Matter*, 2020, **3**, 892–903.
37 A. Schmitz, L. L. Schaberg, S. Sirotinskaya, M. Pantaler, D. C. Lupascu, N. Benson and G. Bacher, *ACS Energy Lett.*, 2020, **5**, 559–565.
38 Y. El Ajjouri, V. S. Chirvony, N. Vassilyeva, M. Sessolo, F. Palazon and H. J. Bolink, *J. Mater. Chem. C*, 2019, **7**, 6236–6240.

 This journal is © The Royal Society of Chemistry 2023

Published on 23 February 2023. Downloaded on 9/20/2024 12:31:46 AM.

39 S. Wu, W. Li, J. Hu and P. Gao, *J. Mater. Chem. C*, 2020, **8**, 13603–13611.
40 S. Fang, T. Wang, S. He, T. Han, M. Cai, B. Liu, V. I. Korepanov and T. Lang, *Phys. Chem. Chem. Phys.*, 2022, **24**, 9866.
41 H. Zhang, J. Yao, Y. Yang and H. Fu, *Chem. Mater.*, 2021, **33**, 2847–2854.
42 X. Wang, N. Ali, G. Bi, Y. Wang, Q. Shen, A. Rahimi-Iman and H. Wu, *Inorg. Chem.*, 2020, **59**, 15289–15294.
43 N. P. Holzapfel, J. D. Majher, T. A. Strom, C. E. Moore and P. M. Woodward, *Chem. Mater.*, 2020, **32**, 3510–3516.
44 E. Sartori, M. Campolucci, D. Baranov, M. Zeng, S. Toso, G. Divitini, M. Ferretti, Z. Hens, L. Manna and F. Locardi, *Nanoscale*, 2022, **14**, 305–311.
45 R. Zhang, Z. Wang, X. Xu, X. Mao, J. Xiong, Y. Yang and K. Han, *Adv. Opt. Mater.*, 2021, **9**, 2100689.
46 C. Zhang, M. Zhang, W. Zheng, J. Wei, S. Wang, P. Huang, X. Cheng, T. Dai, Z. Chen and X. Chen, *Nano Res.*, 2021, **15**, 179–185.
47 Y. Gao, Y. Cui, J. Li, Y. Xu, J. Hu and T. He, *J. Phys. Chem. C*, 2022, **126**, 6694–6699.
48 Z. Ma, Z. Shi, C. Qin, M. Cui, D. Yang, X. Wang, L. Wang, X. Ji, X. Chen, J. Sun, D. Wu, Y. Zhang, X. J. Li, L. Zhang and C. Shan, *ACS Nano*, 2020, **14**, 4475–4486.
49 F. Zhang, D. Yang, Z. Shi, C. Qin, M. Cui, Z. Ma, L. Wang, M. Wang, X. Ji, X. Chen, D. Wu, X. Li, L. Zhang and C. Shan, *Nano Today*, 2021, **38**, 101153.
50 L. Zhou, J. F. Liao, Y. Qin, X. D. Wang, J. H. Wei, M. Li, D. B. Kuang and R. He, *Adv. Funct. Mater.*, 2021, **31**, 2102654.
51 J. G. Hou, S. Y. Cao, Y. Z. Wu, Z. M. Gao, F. Liang, Y. Q. Sun, Z. S. Lin and L. C. Sun, *Chem. – Eur. J.*, 2017, **23**, 9481–9485.
52 Z. C. Kong, J. F. Liao, Y. J. Dong, Y. F. Xu, H. Y. Chen, D. B. Kuang and C. Y. Su, *ACS Energy Lett.*, 2018, **3**, 2656–2662.
53 W. C. Oh, M. Chen, K. Cho, C. Kim, Z. Meng and L. Zhu, *Chin. J. Catal.*, 2011, **32**, 1577–1583.
54 T. G. Asere and G. D. Laing, *Environ. Technol. Innovation*, 2020, **20**, 101126.
55 S. Ahmed, M. G. Rasul, R. Brown and M. A. Hashib, *J. Environ. Manage.*, 2011, **92**, 311–330.
56 C. C. Wang, C. K. Lee, M. D. Lyu and L. C. Juang, *Dyes Pigm.*, 2008, **76**, 817–824.
57 X. Qian, Z. Chen, X. Yang, W. Zhao, C. Liu, T. Sun, D. Zhou, Q. Yang, G. Wei and M. Fan, *J. Cleaner Prod.*, 2020, **249**, 119335.
58 K. A. Sultana, M. T. Islam, J. A. Silva, R. S. Turley, J. A. Hernandez-Viezcas, J. L. Gardea-Torresdey and J. C. Noveron, *J. Mol. Liq.*, 2020, **307**, 112931.
59 X. Lang and J. Zhao, *Chem. – Asian J.*, 2018, **13**, 599–613.
60 B. Tian, R. Dong, J. Zhang, S. Bao, F. Yang and J. Zhang, *Appl. Catal., B*, 2014, **158**, 76–84.
61 K. Katsiev, G. Harrison, H. Alghamdi, Y. Alsalik, A. Wilson, G. Thornton and H. Idriss, *J. Phys. Chem. C*, 2017, **121**, 2940–2950.
62 T. S. Natarajan, M. Thomas, K. Natarajan, H. C. Bajaj and R. J. Tayade, *Chem. Eng. J.*, 2011, **169**, 126–134.
63 K. Yu, S. G. Yang, H. He, C. Sun, C. G. Gu and Y. M. Ju, *J. Phys. Chem. A*, 2009, **113**, 10024–10032.
64 J. Chen, X. Xiao, Y. Wang and Z. Ye, *Appl. Surf. Sci.*, 2019, **467**, 1000–1010.
65 Z. He, C. Sun, S. Yang, Y. Ding, H. He and Z. Wang, *J. Hazard. Mater.*, 2009, **162**, 1477–1486.